ARMA 24–0788

A Study of Rock Breakage under Extreme Submerged Confining Pressure: Can DTH Hammer Drilling Deliver?

Gerbaud, L., Velmurugan N., Aising J. and Chambres C.,
Centre de Géosciences, Mines Paris - PSL University, 77300 Fontainebleau, France
Naderi S., Latham J.P., Xiang J. and Yang X.
Imperial College of London, London, United Kingdom

This paper was prepared for presentation at the 58th US Rock Mechanics/Geomechanics Symposium held in Golden, Colorado, USA, 23-26 June 2024. This paper was selected for presentation at the symposium by an ARMA Technical Program Committee based on a technical and critical review of the paper by a minimum of two technical reviewers. The material, as presented, does not necessarily reflect any position of ARMA, its officers, or members.

ABSTRACT: Drilling cost is one of the main obstacles hindering the development of deep geothermal energy, especially in hard granite formations at great depths. In ORCHYD, an H2020 project, we develop an innovative drilling technology that merges percussion drilling and high-pressure water jetting for drilling hard crystalline rocks. In laboratory, we have demonstrated a fourfold improvement in drilling performance when contrasted with conventional techniques. This article delves into the study of impact of realistic operational conditions, characterized by high in-situ confining stress and hydrostatic pressure, on the drilling technique.

We study variables affecting the mud hammer's performance. Experimentally, our drilling test laboratory houses a set-up designed to dissect the mechanisms of rock fracture during indentation under realistic downhole conditions. Numerically we harnessed our in-house rock fracture software, SOLDITY that leverages a hybrid FDEM method to simulate the intricate interactions of rocks under confining pressures.

Our analysis of experimental and numerical data centered on rock fractures. Our findings show that breaking rock can be 2-3 times more challenging under higher confinement compared to lower confinement conditions. This insight has significant implications for optimizing ORCHYD techniques, improving the efficiency of rock destruction.

1. INTRODUCTION

Geothermal energy is positioned as one important component in the drive to achieve Net Zero Emissions (NZE) by 2050, offering a clean, sustainable, and reliable source of renewable energy. Nevertheless, the high costs associated with geothermal drilling pose a significant obstacle to its widespread adoption and scalability (Angelone, 2014). The primary cost driver in deep geothermal drilling stems from the necessity to penetrate deep and dense crystalline rock formations, such as granites, typically located at depths exceeding 4 km. Deeper drilling not only escalates operational expenses but also demands a substantial increase in the energy required to break rocks under extreme confining stresses and hydrodynamic pressures.

Conventional rotary drilling, such as roller cone and polycrystalline diamond carbide (PDC) bits, encounter difficulties penetrating hard formations like granite, resulting in sluggish rate of penetration (ROP) (Cardoe et al., 2021; Baujard et al., 2017). Percussion drilling, characterized by its effectiveness in penetrating hard formations, has garnered considerable attention in deep geothermal industry, specifically for basement drilling. Despite its advantages, such as enhanced rock penetration and reduced drilling costs, percussion drilling encounters limitations, notably in achieving higher ROP under high confining conditions dictated by geological stresses and mud pressure in the wellbore (Gnirk and Cheatham, 1965; Han et al., 2006).

Percussion drilling involves inducing stress waves via a Down-the-hole (DTH) hammer to facilitate rock penetration, with material removal achieved through rock crushing and lateral crack coalescence. A series of impacts are generated by an oscillating piston, striking a drill bit at frequencies of 20–30 Hz with velocities around 10 m/s. The generation of compressive waves during each impact aids in the penetration of the drill bit by causing indentations on the rock surface (Hartman, 1959). Recent innovations in DTH hammer and percussive drill bit design have led to improvements in drilling efficiency and velocity (Nguyen et al., 2016; Souchal et al., 2017; Gerbaud et al., 2022).

The mechanical behavior of bedrock is significantly influenced by hydrostatic or confining pressure, with compressive strength increasing under such pressure (Hokka et al., 2016). Deep drilling operations accompanied by high pressures, impact rates, and temperatures often result in low ROP (Cunningham, 1959). While there exists a plethora of literature on the effect of impact parameters at atmospheric pressure, only a few authors have studied the effect of confining pressure on rock fracturing during impact. These include Fourmeau et al., (2015) who examined experimentally and numerically the impact of additional confining pressure on the volume of rock removed during drilling. Li et al., (2021) shows experimentally that the confining pressure has a significant effect on the fracture of the rock reporting a 91.5% reduction in the volume destroyed at 20 MPa of confining pressure compared with the volume destroyed at atmospheric pressure. He explains that confining pressure inhibits the propagation of lateral cracks and the extension of radial cracks. Aldannawy et al., (2022) obtained similar results with confining pressures up to 30 MPa observing a fast decrease of drilled volume between 0 and 10 MPa and then, a slow decrease of performance for further increase in confining pressures. It was also shown that the shape of the insert has a large impact on the fracturing of the rock.

This paper explores recent advancements and challenges in percussion drilling, with a focus on understanding the mechanical responses of granite to various operating parameters of percussion drilling, particularly in the presence of varying confining pressures. Studies on rock failure mechanisms and the influence of confining pressure on drilling performance are highlighted with new experimental work provided under confining pressure up to 40 MPa. In order to extend the analysis to deeper geothermal reservoirs, numerical modeling, once validating with the experimental results at medium confining pressure, is used to provide new highlights for deeper reservoir exploration with percussive drilling.

2. EXPERIMENTAL APPROACH

2.1. Experimental Setup

Mines Paris has modified an existing device to enable impact tests to be carried out under confining pressures (Figure 1). The rock (1) is placed inside a pressure cell that can apply a hydrostatic pressure of up to 40 MPa. The fluid used is EDC 95-11 oil. The insert (2), placed at the end of a solid cylindrical rod (3) with a diameter of 50 mm, is held in contact by nitrogen pressure applied in the pressure chamber (4). The 5 kg piston, released from a certain height, impacts the upper part of the rod located outside the cell. Finally, the pressure cell is fitted with 3 safety glass portholes that allow the fracturing of the rock to be viewed during the impact under confined pressure conditions. To determine the impact energy, the impact speed of the piston on the rod is determined using a high-speed 1000 fps camera. An ultra-fast camera (5) recording at 11,000 fps was used to record the displacement of the insert and its speed during impact. Finally, 3 strain gauges (6) placed at different heights on the tool are used to record the compression wave and its reflection during impact.

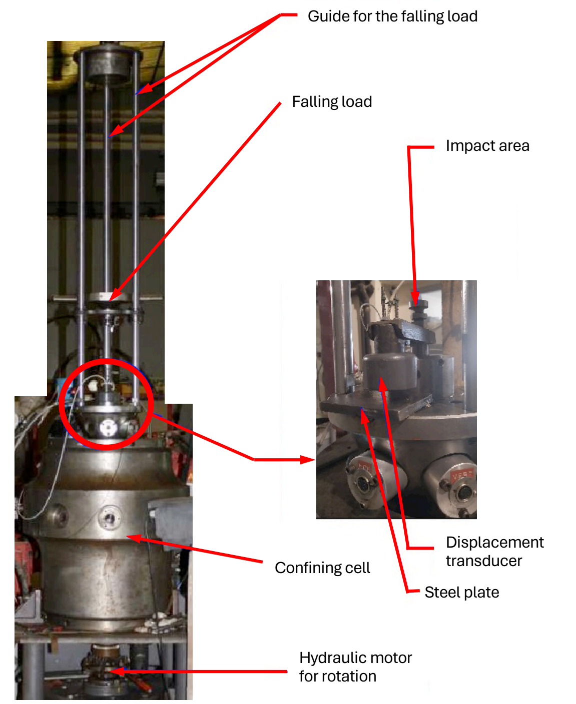

(a) Modified experimental setup containing the guidelines for the impacting load and additional instrumentation.

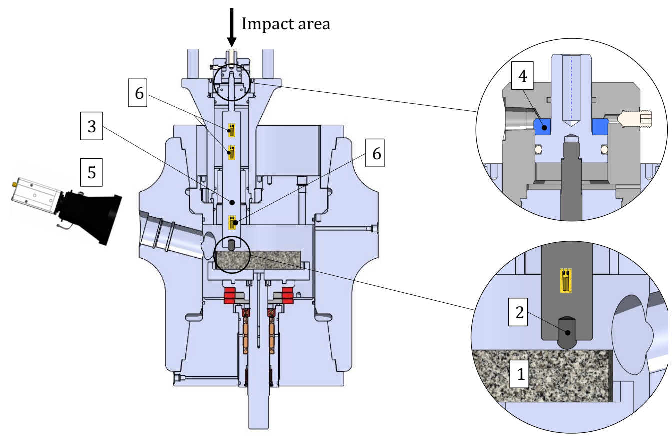

(b) Cross sectional view of the confining cell where the rock samples are pressurized, and strain gauges are placed.

Fig. 1. Experimental setup to carry out impact tests under confining pressures.

2.2. Tested Rock Properties

The experiments were conducted on hexagonal prism specimens of rock blocks of 5 cm height and 12.5 cm edges (Figure 2). Sidobre granite was considered as the primary rock type for experimental tests and numerical model validation. Additional tests were performed using Kuru Grey granite to conduct preliminary sensitivity analysis of operational parameters. Rock mechanical characteristics for the two granites can be found in Table 1. Sidobre granite is a coarse-grained granite with an unconfined compressive strength (UCS) of 154 MPa while Kuru Grey granite is a fine-grained granite with a slightly higher UCS of 186 MPa and highest Brazilian Tensile Stress of 11.3 MPa. Virgin rock samples (with no particular surface preparation) were chosen in this study to provide more confidence in validating the numerical models. Although repeated impacts may weaken the rock, at least on the rock surface and at atmospheric pressure conditions, it is difficult to estimate the level of damage to feed into the model.

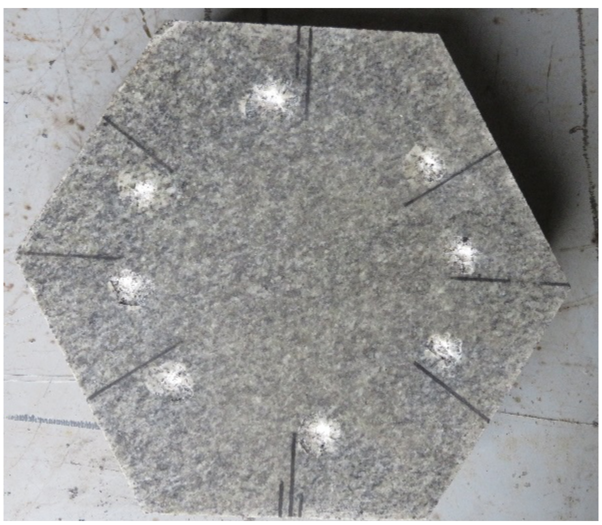

Fig. 2. Top view photograph of the Kuru Grey granite rock sample after a single insert impact test under confining conditions.

Table 1. Mechanical characteristics of Sidobre and Kuru Grey Granites.

Name of Rock	UCS (MPa)	BTS (MPa)	Grain size min-max (mm)
Sidobre	154	10.4	2 – 10
Kuru Grey	186	11.3	0.3 – 1.5

2.3. Data Collection and Processing

- Crater characteristics

After each test, the rock sample is removed from the cell, cleaned and the craters obtained are photographed (Figure 3) and are laser scanned to determine the imprint left by the impact (See Aldannawy et al., (2022) for more details). The geometry of the crater is reconstructed and meshed with CloudCompare software to determine its depth, surface area, and volume (Figure 4).

Fig. 3. Photograph of the crater in Sidobre granite created due to impact of single insert under confining conditions.

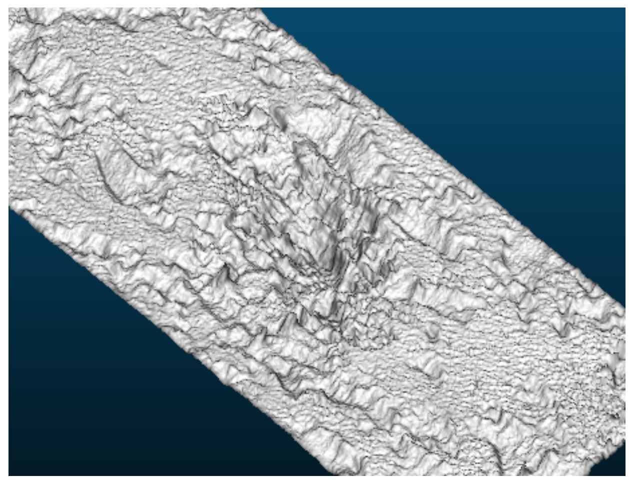

Fig. 4. Visualisation of a Sidobre crater from Fig. 3 using CloudCompare.

- Impact characteristics

The ultra-fast video captured during the impact event undergoes meticulous analysis wherein the movement of the insert is tracked frame by frame utilizing Kinovea software. As depicted in Figure 5, a representative example of insert movement during impact is illustrated while Figure 6 presents a closer look at the initial indentation. At the beginning of the impact, the insert penetrates the rock with a maximum penetration of 0.8 mm at 0.53 ms with an indention impact speed V_{ind} (~2.33 m/s). The insert then rebounds at a speed V_{reb} ($\leq V_{ind}$) and detaches from the rock surface at 0.97 ms. We then see several movements of the insert, which finally stabilizes at a depth of around 0.1 mm. Analysis of the video shows that no fractured rock was ejected from the impact zone, probably because the rock is held in place due to the fluid confining pressure. This is confirmed by the residual penetration after impact, which is virtually zero.

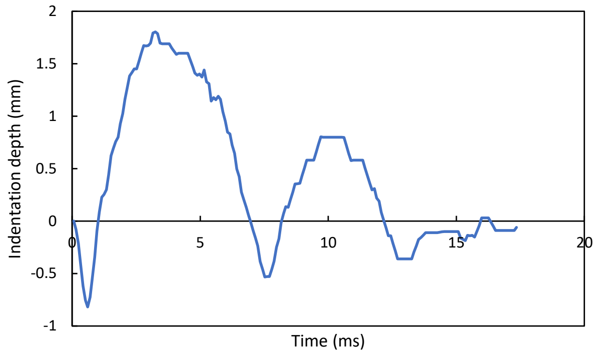

Fig. 5. Time evolution of axial displacement of the insert during percussive impact in Sidobre granite.

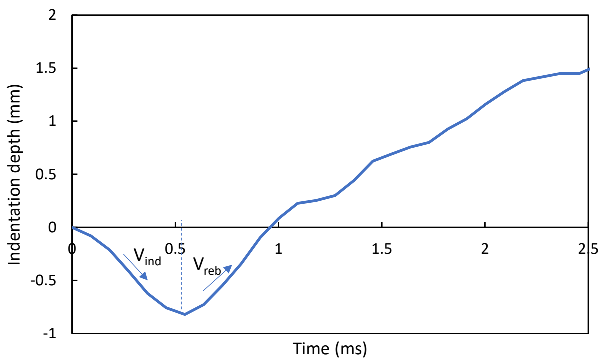

Fig. 6. A zoomed-in view of Fig. 5 providing indentation curve during the first impact.

2.4. *Experimental results*

- Effect of rock heterogeneity

To investigate the influence of rock composition and the variability in experimental outcomes, a series of eight tests were conducted under identical conditions, maintaining constant parameters within a set: an impact energy of 39 Joules, a confinement pressure of 20 MPa, an axial force of 1000 N applied to the insert and a losange piston shape. The outcomes, depicted in Figure 7 present measurements of both the impacted volume and the maximum depth of the resulting crater. Notably, there exists a considerable dispersion in the results, with deviations exceeding 30% from the mean excavated volume of 127 mm^3 and around 20% from the mean penetration depth of 3.1 mm. The observed variations encompass minimum to maximum values spanning from singular instances to more than double. This variance is primarily attributed to the location of impact and the specific mineral composition affected. Al dannawy (2021) highlighted that the impact zone operates at the millimeter scale, akin to the characteristic dimensions of the diverse minerals comprising the Sidobre granite. Consequently, a substantial divergence is evident depending on whether the impact targets quartz, mica, or feldspar constituents.

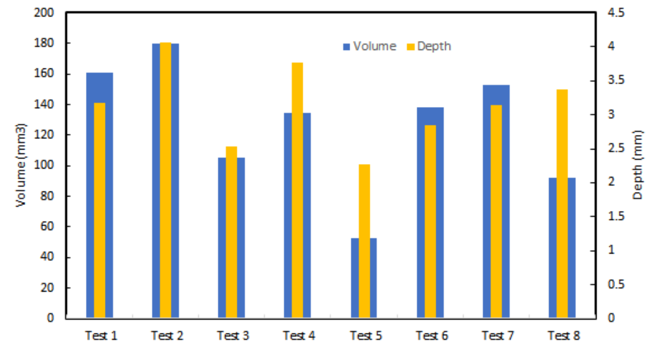

Fig. 7. Repeat tests in Sidobre granite at 39 Joules of impact energy.

- Effect of confining pressure

The impact of varying confining pressure was investigated on two types of granite by adjusting the pressure within the range of 10 to 30 MPa with an impact energy of 39 Joules on the cylindrical piston.

For the same testing conditions, there exists difference in the results obtained in Figure 7 and Figure 8 as two different pistons were used. However, the influence of the piston shape on the rock breakage is beyond the scope of the current study.

The results reveal a pronounced influence of confinement pressure on the coarse-grained Sidobre granite, wherein there is a notable decrease in the destroyed volume with increasing pressure, as illustrated in Figure 8. This observation is consistent with that reported in the literature such as Wu et al (2021). Concurrently, both surface area and penetration depth exhibit a corresponding decrease following this trend. However, it is noteworthy that the reduction in penetration depth is relatively less significant compared to the decrease in destroyed volume or surface area. One potential explanation of this phenomenon is that as the rock is compressed by the confining pressure, inhibiting the extension and propagation of side and lateral cracks, resulting in their shortened length. With shorter side and radial cracks, there is limited coalescence of cracks and reduced formation of fragments, ultimately resulting in a decrease in the size of the crater and of the volume destroyed. On another hand, the zone under the insert is subject to high compressive stresses during impact, and there is a heavily crushed zone directly under the insert. The other well-known effect is the increase in effective compressive strength of the rock with an increase of confining pressure, limiting the rock penetration by an insert with given impact energy. These observations indicate that, for the Sidobre granite, the application of confining pressure significantly affects the propagation of lateral and radial cracks, leading to a threefold reduction in the destroyed volume, while the reduction in indentation depth amounts to only 0.14 mm (equivalent to 5% of the penetration observed at 10 MPa confinement).

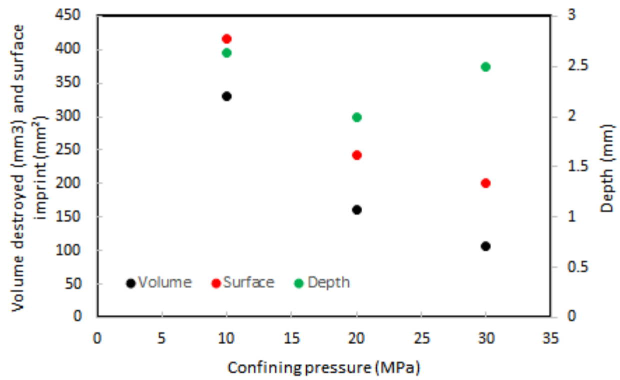

Fig. 8. Evolution of impact crater characteristics evolution with confining pressure for Sidobre granite.

The influence of confining pressure on the fine-grained Kuru Grey granite mirrors the observed trend in the Sidobre granite, characterized by diminishing volume, surface area, and depth, albeit to a lesser degree (Figure 9). Notably, the reduction in excavated volume exhibits a lower magnitude (with a ratio of 2) compared to the Sidobre granite (ratio of 3), whereas the decrease in depth is more pronounced. One possible reason for this is the greater ease with which lateral and radial cracks propagate in the Sidobre granite beyond the area impacted by the cutter. In fact, we can see that the depth of indentation between the two granites is similar, whereas the volume cut is different and much greater in the Sidobre granite. It is therefore normal that the effect of the confining pressure, which has the effect of limiting the propagation of lateral and radial cracks, should be more pronounced in the Sidobre granite.

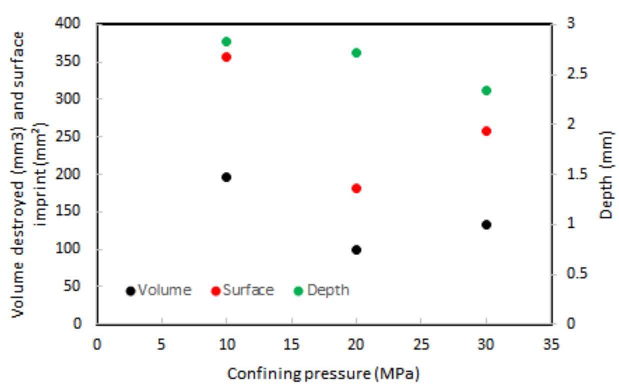

Fig. 9. Evolution of impact crater characteristics evolution with confining pressure for Kuru Grey granite.

Additionally, and for the same reasons, there appears to be an accelerated approach towards an asymptotic value in the volume destroyed. However, to substantiate this hypothesis, further experimentation is warranted, accounting for the effects of heterogeneity and the associated dispersion of results. Nevertheless, it seems that the effect of confining pressure is greater for coarse-grained granites.

3. NUMERICAL APPROACH: FDEM SIMULATION FOR ROCK BREAKAGE ANALYSIS USING SOLIDITY

3.1. Introduction to FDEM

A hybrid Finite Element and Discrete Element Method (FDEM) to simulate the complex dynamics of insert-rock interaction under both impact and extreme confining pressure, conditions that are challenging to replicate in laboratory settings. FDEM stands as a well-established computational technique renowned for its capability to explicitly model the discrete fracture behavior and fragmentation mechanisms inherent in brittle materials such as rock. Moreover, its robustness extends to encompassing mechanical contact problems, notably those arising from impact scenarios. The FDEM software SOLIDITY, developed by Imperial College London, was utilized for this study.

In FDEM, the fracture domain is conceptualized as a multi-body system, wherein each discrete element undergoes further discretization into finite elements. This approach enables the analysis of both discontinuum behavior, such as multi-body interactions and contacts at fracture surfaces, and continuum behavior, encompassing deformation and stress within discrete elements. Initially, the intact material is modeled as a continuum using Finite Element Method (FEM). Upon fracture initiation, a hybrid representation of continua and fractures is adopted, with FEM handling the continua and Discrete Element Method (DEM) managing the interaction between discrete fracture surfaces through contact algorithms. Joint elements are endowed with deformation and strength parameters, with their failure indicating crack initiation. Additionally, the DEM formulation allows for handling large displacement problems efficiently.

The FDEM method, introduced by Munjiza (2004), has found extensive application across a spectrum of engineering challenges, as demonstrated by Xiang et al. (2009), Lei et al. (2014), and Mahabadi et al. (2012). A comprehensive elucidation of the 3D fracture model integrated into SOLIDITY was summarized in Guo et al. (2015, 2020). Furthermore, a mesh sensitivity study of SOLIDITY FDEM was conducted by Guo et al. (2016).

3.2. Model Setup

- Material model

A nonlinear Mohr-Coulomb criterion, accounting for high confining pressures and featuring a tension cut-off, governs the shear strength based on the normal stress perpendicular to the shear direction. This criterion describes the stress evolution process, wherein initially, stress increases elastically with joint aperture until it reaches a predetermined strength threshold.

Subsequently, the material undergoes a nonlinear strain-softening stage.

To address the high strain rate conditions inherent in impact events, a Dynamic Increase Factor (DIF) is incorporated into the material model. The DIF models are defined by Eqs. (1) and (2) for compression and tension modes, respectively, as functions of strain rate ($\dot{\varepsilon}$). The DIF_c is applied to cohesion and fracture energy release rate in mode II (G_{II}); and DIF_t are applied to tension and fracture energy release rate in mode I (G_I). It is worth mentioning that consistent with the theoretical framework advanced by Zhao (2000), the impact of the internal friction coefficient on strain rate is considered negligible within this modeling framework.

$$DIF_c = \begin{cases} 1, & \dot{\varepsilon} \le 5 \times 10^{-6} \\ 0.77 + 0.56\dot{\varepsilon}^{0.07}, & 5 \times 10^{-6} < \dot{\varepsilon} \le 10^4 \\ 1.84, & 10^4 < \dot{\varepsilon} \end{cases} \quad (1)$$

$$DIF_t = \begin{cases} 1, & \dot{\varepsilon} \le 5 \times 10^{-6} \\ 0.95 + 0.41\dot{\varepsilon}^{0.17}, & 5 \times 10^{-6} < \dot{\varepsilon} \le 10^2 \\ 1.85, & 10^2 < \dot{\varepsilon} \end{cases} \quad (2)$$

The material and contact parameters used in the simulations are detailed in Table 2 for Sidobre granite and bit. The values for mechanical and physical properties, apart from energy release rates of the rock, were derived from typical engineering properties obtained through experimental investigations or drawn from literature reporting FDEM-based simulations for hard rock materials and steel. The values for G_I and G_{II} were determined via a calibration process, which will be elaborated upon later, using a trial-and-error method. The bit is treated as a fracture-free component.

- Geometry, boundary and loading conditions

In the numerical simulation, a two-body system representing the rock-bit interaction was proposed, in contrast to a three-body system involving piston-bit-rock interaction, as illustrated in Figure 1. This approach was adopted due to the complex nature of the confining pressure apparatus within the experimental setup, wherein full replication within the simulation framework is challenging and may introduce uncertainties. Thus, to minimize potential discrepancies, the simulation focused solely on modeling the interaction between the bit and the rock.

Two structural configurations are considered to represent both laboratory and in-situ field conditions. Figure 10 schematically illustrates the model geometry and boundary conditions. This approach enables validation of the model against laboratory setups under a hydrostatic pressure (P_h) of 20 MPa, and subsequently exploring conditions beyond laboratory limits at 50, 100, and 130 MPa. In order to ensure comparability between laboratory experimental results and field conditions, the in-situ models are designed to uphold a constant mud pressure (P_m) of 50 MPa. The confining pressure (P_c), as depicted in the figure, increases from 50 to 100 and 130 MPa, the latter being indicative of in-situ pressures at a depth of 5 km. Careful consideration of dimensions ensures the creation of a sufficiently large confined zone around the impact point at the targeted pressure level. Considering the applied body forces and pressures across various components, the pull-down force – i.e., the effective Weight on Bit (WoB) – was adjusted to 100 kg.

Table 2. Material and contact parameters used in FDEM simulations for Sidobre Granite and Bit.

	Parameters	Value
Rock (Sidobre Granite)	Density (kg/m^3)	2626.00
	Young's Modulus (GPa)	30.00
	Poisson's Ratio (Pa)	0.20
	Mass Damping Coefficient	3000.00
	Penalty Number (GPa)	6000.00
	Energy Release Rate Mode I (J·m^{-2})	10.00
	Energy Release Rate Mode II (J·m^{-2})	50.00
	Tensile Strength (MPa)	10.32
	Cohesion (MPa)	25.84
	Internal Friction	1.33
	Sliding Friction Coefficient (Rock-Rock)	0.60
Bit (Steel)	Density (kg/m^3)	7268.77
	Young's Modulus (GPa)	200.00
	Poisson's Ratio (Pa)	0.30
	Mass Damping Coefficient	2000.00
	Penalty Number (GPa)	3000.00
	Sliding Friction Coefficient (Bit-Rock)	0.01

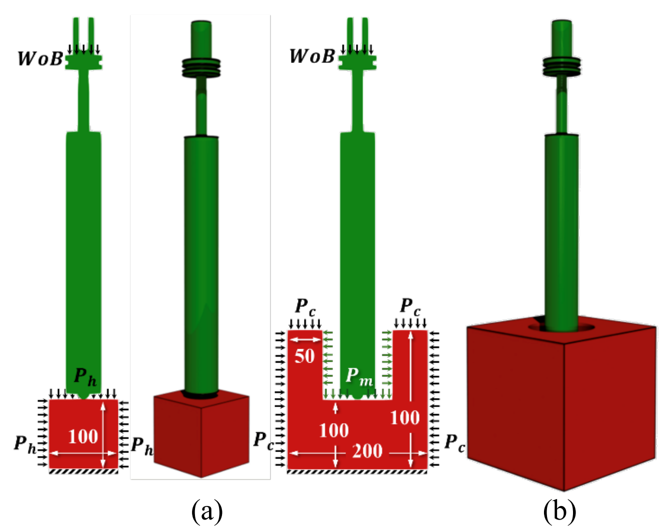

Fig. 10. Schematic representation of geometry and boundary conditions depicting (a) laboratory and (b) field conditions.

According to the experimental studies, the initial velocity of the bit remains for all models, set at 2.33 m/s, corresponding to an initial impact energy of 16.36 J. The energy losses in the system can be attributed to two reasons: 1) As the impact takes place outside the pressurized cell in the three rigid body test, we assume a loss of energy at the top sealing system (tight O-ring), and 2) We assume a damping effect during the impact due to the fluid layer between the end of the rod surrounding the insert and the rock. Furthermore, movement of the bit is restricted solely to the axial direction, while the lower boundary of the rock model was clamped.

The unstructured mesh was constructed using linear tetrahedral elements. Finer elements, with an average size of 1 mm, were concentrated around the impact point. This mesh refinement ensures computational accuracy in capturing high strain loading impacts. Importantly, this size is smaller than the minimum grain size of Sidobre granite.

- Computational setup and solution approach

The FDEM problem is addressed through an explicit numerical solution, employing a time step of 10^{-9} seconds. This step size is chosen to stabilize the solving process while simultaneously mitigating unnecessary computational overhead. The numerical model progresses through three distinct phases: (i) initially, pressure and force are gradually increased on the boundaries until reaching target values. This phase aims to capture the transient dynamic response of the system; (ii) following the boundary preparation, the simulation proceeds to the impact event, simulating the interaction between the bit and the rock; and (iii) finally, a mass removal process is simulated to emulate the chipping removal mechanism observed in reality. This phase involves applying a force similar to anti-gravity to the rock, enabling the identification of “removable” cuttings. The accurate interpretation of geometric characteristics of the simulated crater is very important to ensure that the comparison with experimental data and validation is objective.

3.3. Simulation Results and Discussion: Extension to Deep Drilling Conditions

The subsequent section provides a comprehensive analysis of the simulation results, encompassing key aspects such as cracks and fragmentation, crater characteristics, energy damage parameters, total crack area, dynamic motion of the bit, and contact force on the tip of the insert. Furthermore, the simulation results will undergo comparison and validation against experimental findings. For validation purposes, numerical results will be compared with the mean values derived from the experimental dataset, considering that homogeneous material was employed in the simulation. However, it is important to note that while the simulation accounts for homogenous material, the use of unstructured mesh in FDEM models inherently introduced some degree of rock heterogeneity into the model.

- Analysis of crater and fragmentation morphology

Figure 11 and Figure 12 illustrate the crack network and fragmented zones (shown in red) formed across the network, alongside the removable chippings (depicted in green) in the upper rows, representing laboratory hydrostatic and in-situ conditions, respectively, with a cross-sectional view. For each case, the maximum depth of the fragmented zone (denoted as d_f) and craters (denoted as d_c) are provided. Furthermore, in the lower rows, the crater morphology is shown by removing the removable chippings from the rock, shown from an upper view.

The d_c for the hydrostatic case under 20 MPa serves as the reference case for validation, with a measurement of approximately 3.3 mm, closely aligning with the experimental result of 3.14±0.59 mm. Notably, an increase in confining pressure to 130 MPa results in a shallower crater depth, reduced by approximately 24% and 66% for the hydrostatically confined case and in-situ conditions, respectively. Similarly, the depth of the fragmented zone (d_f) experiences a decrease of approximately 39% and 26%, respectively. Moreover, it is observed that the depth parameters tend to stabilize under high confining pressures. For the in-situ models exceeding 100 MPa, the crater depth approaches the scale of an element, suggesting the possibility of no crater formation per impact for intact hard rock such as Sidobre. However, evidence of rock fracturing in the vicinity of the impact point is visible through the presence of fragments. To provide a more precise analysis, the volume of the fragmented zone and chipping removal are examined as parameters that offer greater accuracy than depth measurements, which may be influenced by the irregular shape of craters and fragmentation, as well as possible measurement errors.

Figure 13 and Figure 14 illustrate the volumes of chipping removal (v_c) and total fragments (v_f) for the models under hydrostatic and field conditions, respectively. The 3D structures display the accumulated fragments resulting from impact and removable chippings, using a consistent colour code. Regarding the volume parameter, the simulation results (119.02 mm³) closely align with the mass removal measured in the experiment (127.12±41.29 mm³). Similarly to depth, a consistent trend is observed for v_c, with a higher decrease percentage of ~59% and 90% for the hydrostatic and in-situ cases, respectively, upon increasing the confining pressure to 130 MPa. Likewise, for v_f, the decrease is ~70% and 36%. While volume provides a more representative value compared to depth, it may not fully capture the energy dissipated by the crack network system. To further characterize rock fracture behaviour, spatial stress in the rock and bit-rock contact force versus bit displacement, along with energy analysis, are considered in the following discussion, exploring their relationship with crack properties.

- Analysis of stress, contact force-bit displacement and energy damage index

To gain deeper insights into the influence of increasing confining pressure, it is necessary to investigate the interaction between impact-induced stress and confining pressure, unraveling the underlying mechanisms. In Figure 14, the propagation of the relative tensile stress wave (represented by sigma 1) post-impact is shown, with arrows and semi-circles serving as visual aids. This stress wave leads to the formation of a low-confining pressure zone, as evidenced by the region exhibiting relatively lower stress near the impact zone, potentially facilitating crack evolution and fragmentation. As the confining pressure increases, and given a constant impact energy, this effect weakens, resulting in a reduction in the induced low-confining zone and consequently smaller total volumes of fragments. It is worth noting that in Figure 14, the range of sigma 1 is adjusted to accentuate the description presented herein.

The rock-bit contact force and the displacement of the bit provide essential insights into the behavior of rock under impact, potentially reflecting the effects of extreme conditions. Figure 15 illustrates the force-displacement relationship during impact loading, which serves as an indicator of rock impact resistance. A typical indentation/impact profile is shown, characterized by loading and unloading curves. The maximum force (f_{max}) is an indication of impact strength or a form of impact hardness, while the corresponding indentation depth (d_{max}) depicts rock deformation, encompassing elastic, plastic-like (i.e. inelastic), and fracture-based deformations. As observed, the stiffness of the rock, as indicated by the slope of the loading curve, remains relatively unchanged with the increase in confining pressure for both hydrostatic and in-situ conditions. However, it is evident that the material becomes harder, as evidenced by the increase in f_{max} by approximately 23% and 20% for the hydrostatic and in-situ cases, respectively, with pressure raised to 130 MPa. Notably, under field conditions and laboratory conditions, the behavior is nearly identical, unlike the increase observed in d_{max}. Specifically, d_{max} increases by ~21% and 10% for the hydrostatic and in-situ conditions, respectively, suggesting greater deformation. However, given the smaller volume of fragments, this deformation is primarily characterized by elastic-inelastic behavior rather than fracture-based mechanisms. A comparison of the cases under the laboratory and the field conditions reveals that structural effects influence stress distribution, resulting in reduced deformability of the rock. A second observation to note is to the initial nonlinearity at the onset of the loading phase. With increasing pressure, greater nonlinearity (i.e. compliance) is observed, particularly pronounced under hydrostatic pressure conditions. It could be attributed to several potential factors: (i) the heightened pressure conditions may lead to an enlarged contact area between the bit and the rock surface. This expansion in contact area might engender a more intricate stress distribution within the rock, consequently contributing to the observed nonlinearity; and (ii) it could signify the transition from elastic to inelastic deformation within the material. With elevated pressure conditions, the material may undergo a more abrupt shift from elastic to inelastic behavior, thereby intensifying the degree of nonlinearity.

The dissipated energy (E_d) within the rock can be derived from the force-displacement curve as the area enclosed between the loading and unloading phases. This quantity can serve as an impact damage index (DI), defined as the ratio of E_d to the initial impact energy. It offers a more precise quantitative measure compared to the previously discussed volume of fragments. In Figure 16, the damage index is plotted against the confining pressure, alongside the total crack area, representing the energy dissipated during cracking – where the total crack area is obtained by summing the area of all triangulated crack surfaces. Dotted lines are included in the figures to aid visualization. The observed trends align closely with those of v_c and v_f. DI decreases by 26% and 0.04% for hydrostatic and field conditions, respectively, while the crack area decreases by 65% and 20%. This suggests that, given a constant impact energy, the confinement effect is more pronounced for the crack area. Furthermore, under in-situ confining conditions, the level of damage shows minimal change, indicating that while the energy dissipated for fracturing decreases, a relatively greater portion of the energy is utilized for inelastic deformation.

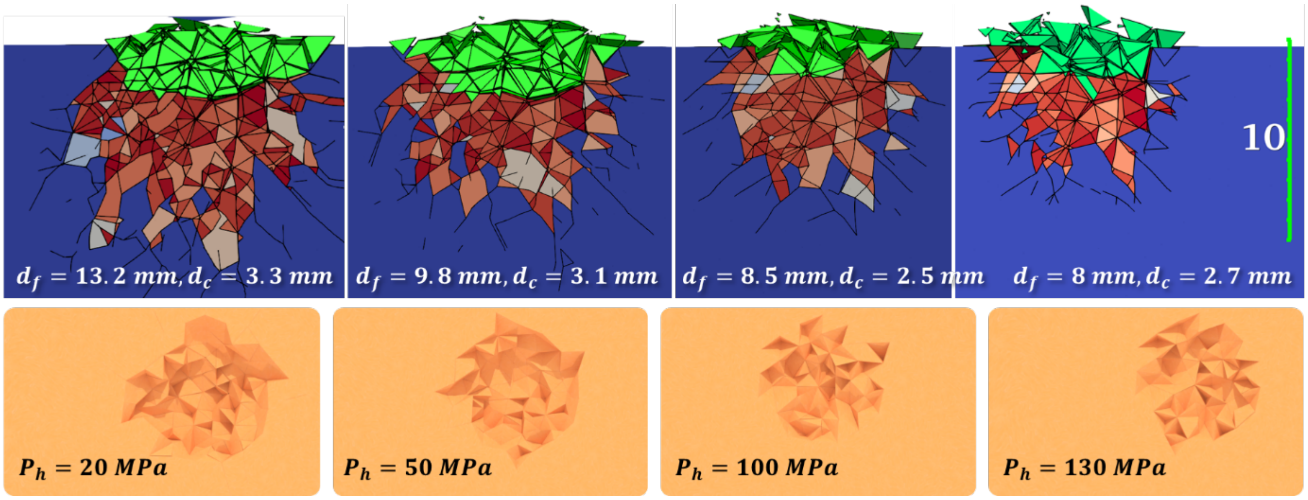

Fig. 11. Upper row: Cross-sectional view depicting simulated cracks, fragmented zone (elements in red), and removable fragments (elements in green); Lower row: Simulated crater after impact, viewed from above. Models subjected to hydrostatic confining (p_h) pressure conditions. d_f and d_c denote the maximum depth of the fragmented zone and crater, respectively.

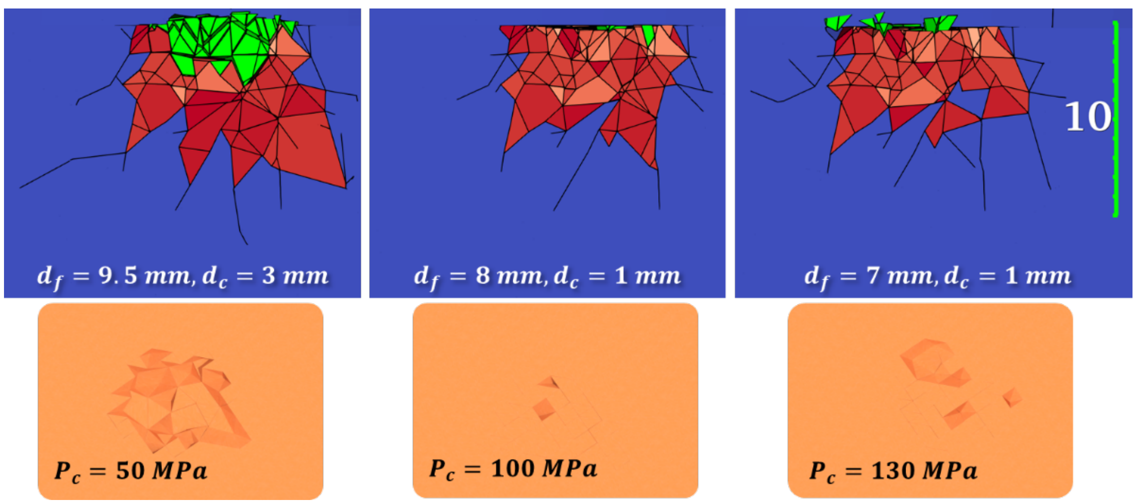

Fig. 12. Upper row: Cross-sectional view depicting simulated cracks, fragmented zone (elements in red), and removable fragments (elements in green); Lower row: Simulated crater after impact, viewed from above. Models subjected to in-situ confining pressure (P_c) and constant mud pressure (P_m) of 50 MPa conditions. d_f and d_c denote the maximum depth of the fragmented zone and crater, respectively.

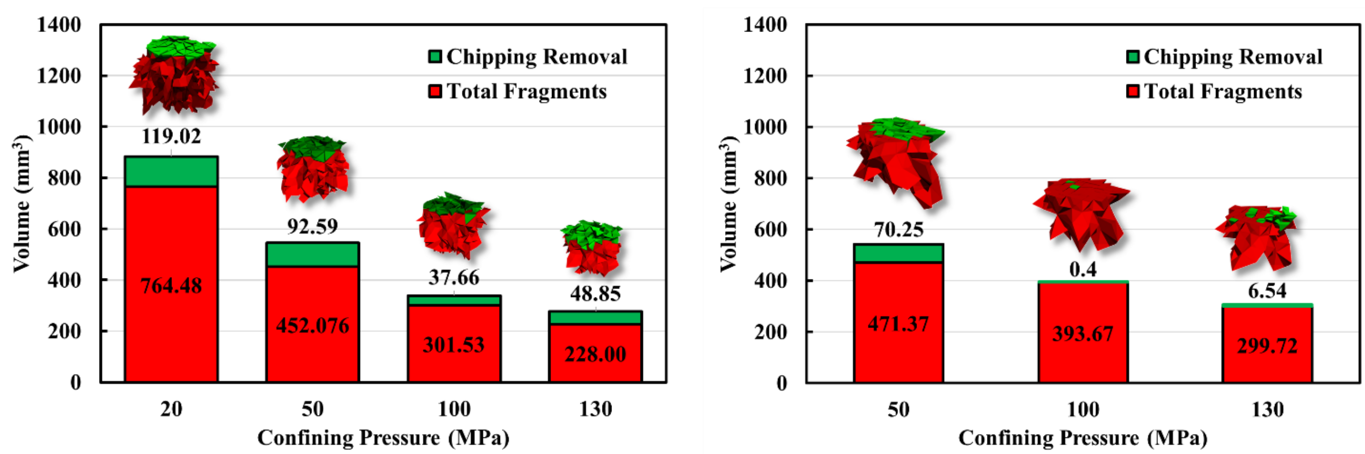

(a) Under hydrostatic confining pressure

(b) Under in-situ confining pressure

Fig. 13. Volume of total fragments and chipping removal.

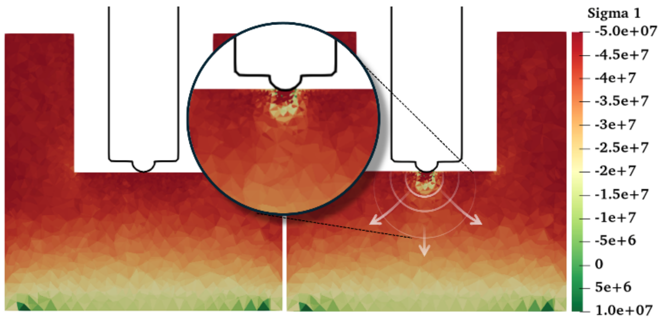

(a) (b)

Fig. 14. Pre-impact stress distribution under confining pressure, and (b) post-impact interaction of tensile stress wave with confining pressure. Arrows and semi-circles illustrate the direction of tensile wave propagation and potential low-confining zone induced. The unit of Sigma 1 is Pa.

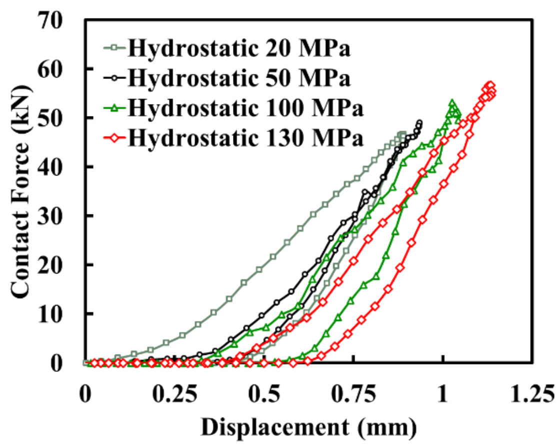

(a) Under hydrostatic confining pressure

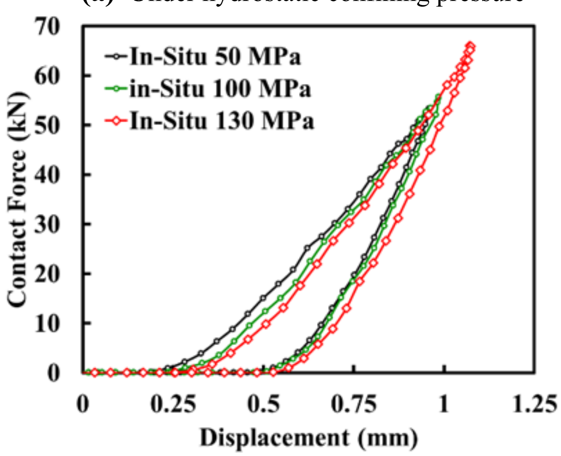

(b) Under in-situ confining pressure

Fig. 15. Contact force versus bit indentation displacement.

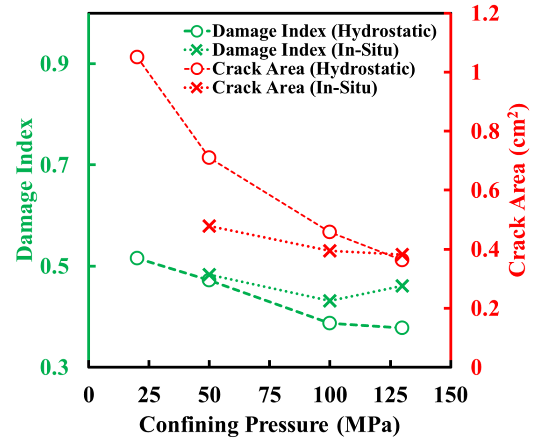

Fig. 16. Damage Index (*DI*) and crack area as a function of confining pressure.

4. CONCLUSIONS

Both Sidobre and Kuru Grey granites were tested experimentally under confining pressures up to 40 MPa. The characteristics of the impact crater were presented as a function of different operational conditions. Due to practical limitations in the laboratory conditions and considering that real downhole conditions are more complex than can be reproduced in a pressure cell, these results were used firstly for validation of numerical models and secondly to simulate field conditions.

The FDEM models were developed for Sidobre granite to simulate the rock response to impact under both hydrostatic confining pressures, representing laboratory conditions, and in-situ field confining pressure, extending up to 130 MPa beyond the laboratory limits. The models accurately captured the fragmentation and mass removal process, closely mirroring real-world phenomena. Furthermore, the simulation results closely matched experimental data regarding the volume and depth of crater formation.

The impact response of Sidobre granite was examined across various parameters, encompassing crater volume and depth, total fragmented volume resulting from impact, total crack area, the introduced energy damage index, stress distribution (sigma 1), contact force, and bit indentation displacement. While crater volume and depth have conventionally served as metrics for assessing impact damage, they are not entirely representative. Other parameters, such as crack area and parameters driven by contact force, offer greater representativeness and are more indicative of impact damage.

To collectively summarize the findings, Figure 17 displays the experimental data points alongside the simulation results for crater volume across a range of confining pressures, including 10, 20, 30, 50, 100, and 130 MPa. The crater volume decreases from 141.90 mm^3 at 10 MPa to 37.66 mm^3at 100 MPa, reflecting a 65% reduction under laboratory conditions (i.e. pressure cell type hydrostatic loading conditions). The suppression of crater formation as a function of confining pressure is more pronounced above 100 MPa. It is particularly significant under in-situ loading conditions, where crater volumes may approach zero per impact on intact rock when confining stresses are in the region of 100 MPa or above, for a bottom hole mud pressure of 50 MPa. Going from 100 to 130 MPa , the rock exhibits a 20% increase in hardness, with an additional 13% increase compared to both hydrostatic and in-situ conditions. This suggests that fracture contributes less to rock deformation and energy dissipation under these conditions.

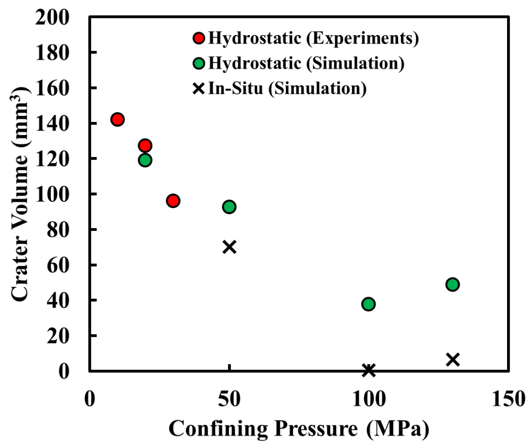

Fig. 17. Experimental and simulation results illustrating the variation in crater volume across different confining pressures.

In forthcoming research, the cumulative influence of repeated impact loading will be investigated to refine crater volume predictions, with the aim of achieving greater correspondence with real-world conditions. Additionally, a broader range of cases will be examined to establish a more comprehensive dataset for regression analysis, facilitating parameterization as a function of confining pressure. Furthermore, investigations into the effects of initial impact energy, rock microstructure (i.e. heterogeneity) and insert shape under such conditions will also be undertaken.

5. ACKNOWLEDGEMENT

This project received funding from the European Union's Horizon 2020 research and innovation program under grant agreement no. 101006752.

REFERENCES

1. Aldannawy, H. A., Rouabhi, A., & Gerbaud, L. (2022). Percussive Drilling : Experimental and Numerical Investigations. Rock Mechanics and Rock Engineering, 55(3), 1555-1570.
2. Aldannawy, H. A., Gerbaud, L., & Rouabhi, A. (2021). On the Influence of Tool Shape on Percussive Drilling in Hard Rocks. ARMA-2021-1145.
3. Angelone M., and Labini S. S. (2014). Energy Research Knowledge Centre – *European Commission*,
4. Baujard, C., Hehn, R., Genter, A., Teza, D., Baumgärtner, J., Guinot, F., ... & Steinlechner, S. (2017). Rate of penetration of geothermal wells: a key challenge in hard rocks. *In Workshop on geothermal reservoir engineering. Stanford University, USA,*
5. Cardoe, J., Nygaard, G., Lane, C., Saarno, T., & Bird, M. (2021). Oil and Gas Drill Bit Technology and Drilling Application Engineering Saves 77 Drilling Days on the World's Deepest Engineered Geothermal Systems EGS Wells., *In SPE/IADC International Drilling Conference and Exhibition. OnePetro*
6. Cunningham, R.A., & Eenink, J.G. (1959). Laboratory Study of Effect of Overburden, Formation and Mud Column Pressures on Drilling Rate of Permeable Formations. Transactions of the AIME, 217, 9-17.
7. Fourmeau M, Depouhon A, Kane A, Hoang H, Detournay E (2015). Influence of indexation and impact energy on bit/rock interface law in percussive drilling: an experimental study. In: U.S. rock mechanics/geomechanics symposium, Paper No. ARMA-2015- 522.
8. Gerbaud, L., Pubill, A., Aldannawy, H., Rouabhi, A., Lamazouade, M., Souchal, R., Cuillier, B., Mud Hammer Drilling in Deep Hard Geothermal formation, from the single impact to the directional and vibration characterization, (2022) *European Geothermal Congress, Berlin*
9. Gnirk, P.F., and J. B. J. Cheatham. (1965), An experimental study of single bit-tooth penetration into dry rock at confining pressures of 0 to 5000psi. *SPE Journal*, 5: 117–130
10. Guo, L., Latham, JP., and Xiang., J. (2015). Numerical simulation of breakages of concrete armour units using a three-dimensional fracture model in the context of the combined finite-discrete element method. *Computers and Structures*, 146:117-142.
11. Guo, L., Xiang., J., Latham, JP., and Izzuddin B. (2016). A numerical investigation of mesh sensitivity for a new three-dimensional fracture model within the combined finite-discrete element method. *Engineering Fracture Mechanics*. 151:70-91.
12. Guo, L., Xiang., J., Latham, JP., and Izzuddin B. (2020). A generic computational model for three-dimensional fracture and fragmentation problems of quasi-brittle materials *European Journal of Mechanics-A/Solids* 84: 104069
13. Han, G.; Bruno, M., (2006), Lab investigations of percussion drilling: from single impact to full scale fluid hammer, *American Rock Mechanics Association*, ARMA-06-962,ARMA
14. Hartman, H., (1959), Basic studies of percussive drilling, *Mining Engineering*, 11: 68–75
15. Hokka, M., J. Black, D. Tkalich, M. Fourmeau, A. Kane, H. Hoang, C. Li, W. Chen, and V.T. Kuokkala, Effects of strain rate and confining pressure on the compressive behavior of kuru granite. International, *Journal of Impact Engineering*, (2016), 91: 183–193.
16. Lei, Q., Latham, J.P., Xiang, J., Tsang, C.F., Lang P. and Guo L. (2014). Effects of geomechanical changes on the validity of a discrete fracture network representation of a realistic two-dimensional fractured

rock. *International Journal of Rock Mechanics and Mining Sciences*. 70:507-523.

17. Li, Y., Peng, J., Zhang, P., & Huang, C. (2021). Hard Rock Fragmentation in Percussion Drilling Considering Confining Pressure : Insights from an Experimental Study. International Journal of Rock Mechanics and Mining Sciences, 148, 104961.
18. Mahabadi, O.K., Lisjak, A., Munjiza, A. and Graselli., G. (2012). Y-Geo: new combined finite-discrete element numerical code for geomechanical applications. *International Journal of Geomechanics,* 12(6):676-688.
19. Munjiza, A. (2004). The combined finite-discrete element method. John Wiley & Sons.
20. Nguyen V.H., Gerbaud, L., Souchal, R., Urbanczyk, C., Fouchard C. (2016). Penetration rate prediction for percussive drilling with rotary in very hard rock. *Vietnam Journal of Science and Technology,* C. Vol 54 No 1
21. Souchal R., Gerbaud L., Tarek M., (2017). High-Power Mud Hammer: A Promising Solution for Hard Formations Drilling. *Abu Dhabi International Petroleum Exhibition & Conference*, Abu Dhabi, United Arab Emirates
22. Wu, G., Liu, K., Hu, W. R., Li, J. C., Dehkhoda, S., & Zhang, Q. B. (2021). Quantification of dynamic damage and breakage in granite under confined indentation. International Journal of Rock Mechanics and Mining Sciences, 144, 104763.
23. Xiang, J., Munjiza, A. and Latham J-P., (2009). Finite strain, finite rotation quadratic tetrahedral element for the combined finite–discrete element method. *International journal for numerical methods in engineering*, 2009. 79(8): 946-978.